Joule

CellPress

Article

Recycled cathode materials enabled superior performance for lithium-ion batteries

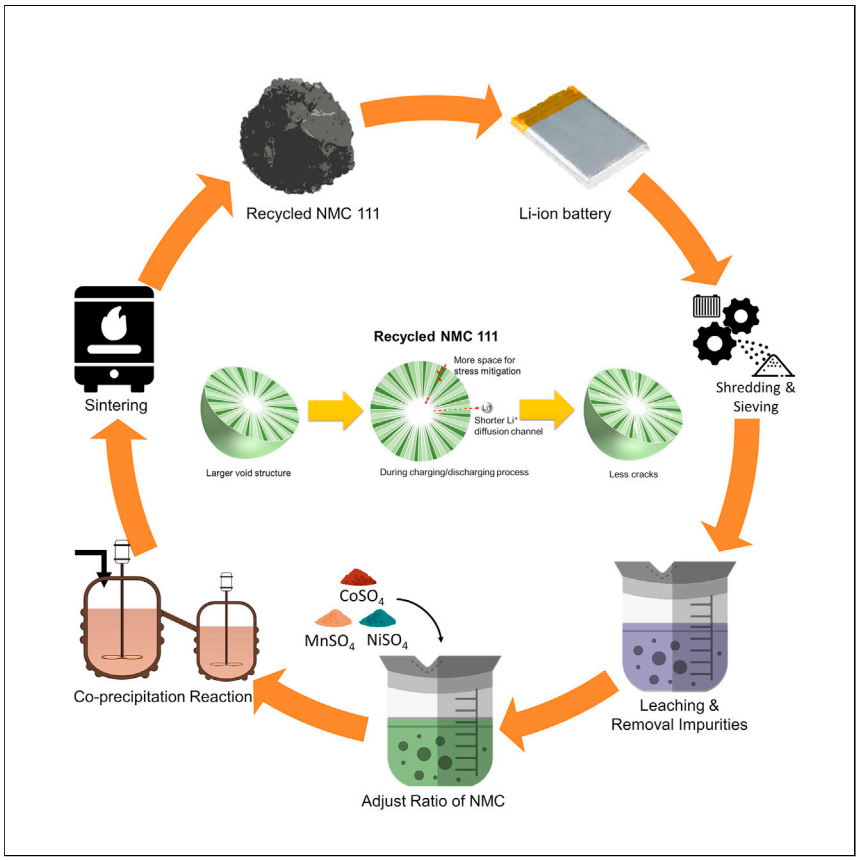

Based on our closed-loop recycling process, recycled NMC111 with unique microstructure has a superior rate and cycle performance, verified by various industry-level tests. Recycled materials' unique void/pore-rich structure provides a higher Li chemical diffusion coefficient and better strain mitigation during cycling, leading to fewer cracks. Thus, our work offers a green and sustainable solution for spent lithium-ion batteries, eliminates industry doubts on the performance of recycled materials, paves the way for lithium-ion battery recycling commercialization, and builds a bridge between industry and academia.

Xiaotu Ma, Mengyuan Chen, Zhangfeng Zheng, ..., Peter Karlson, Nakia Simon, Yan Wang

yanwang@wpi.edu

Highlights

This work eliminates industry doubts about the performance of recycled materials

This work builds a bridge between industry and academia

Based on our recycling process, the recycled materials enable superior performance

The special void/pore-rich structure of recycled materials benefits performance

Ma et al., Joule 5, 2955–2970
November 17, 2021
https://doi.org/10.1016/j.joule.2021.09.005

Joule

CellPress

Article

Recycled cathode materials enabled superior performance for lithium-ion batteries

Xiaotu Ma,[1,9] Mengyuan Chen,[1,9] Zhangfeng Zheng,[1,9] Dennis Bullen,[2] Jun Wang,[2] Chloe Harrison,[2] Eric Gratz,[3] Yulin Lin,[4] Zhenzhen Yang,[5] Youtian Zhang,[6] Fan Wang,[6] David Robertson,[5] Seoung-Bum Son,[5] Ira Bloom,[5] Jianguo Wen,[4] Mingyuan Ge,[7] Xianghui Xiao,[7] Wah-Keat Lee,[7] Ming Tang,[6] Qiang Wang,[1] Jinzhao Fu,[1] Yubin Zhang,[1] Bryer C. Sousa,[1] Renata Arsenault,[8] Peter Karlson,[8] Nakia Simon,[8] and Yan Wang[1,10,*]

SUMMARY

Recycling spent lithium-ion batteries plays a significant role in alleviating the shortage of raw materials and environmental problems. However, recycled materials are deemed inferior to commercial materials, preventing the industry from adopting recycled materials in new batteries. Here, we demonstrate that the recycled $LiNi_{1/3}Mn_{1/3}Co_{1/3}O_2$ has a superior rate and cycle performance, verified by various industry-level tests. Specifically, 1 Ah cells with the recycled $LiNi_{1/3}Mn_{1/3}Co_{1/3}O_2$ have the best cycle life result reported for recycled materials and enable 4,200 cycles and 11,600 cycles at 80% and 70% capacity retention, which is 33% and 53% better than the state-of-the-art, commercial $LiNi_{1/3}Mn_{1/3}Co_{1/3}O_2$. Meanwhile, its rate performance is 88.6% better than commercial powders at 5C. From experimental and modeling results, the unique microstructure of recycled materials enables superior electrochemical performance. The recycled material outperforms commercially available equivalent, providing a green and sustainable solution for spent lithium-ion batteries.

INTRODUCTION

Attributable to their possession of long cycle life and high energy density, lithium-ion batteries (LIBs) are widely employed in our daily lives, such as in consumer electronics, electric vehicles (EVs), and energy storage systems.[1–3] In particular, the yield of LIBs for EVs could reach 0.33 to 4 million metric tons from 2015 to 2040,[4] which will cause concerns about resource supply chain, especially for Co.[1] With increased use, the quantity of spent lithium-ion batteries becomes non-negligible. According to the forecast, 21 million cumulative end-of-life LIBs packs could be generated between 2015 and 2040.[5] Therefore, to ease supply chain pressure, protect the environment, and realize industry sustainability, efficient recycling processes must be developed sooner rather than later.[5]

However, there are concerns about reintroducing recycled materials in industry, and the questions arise from whether recycled materials can compete with commercial control materials in terms of cost, yield, and performance. Academia and industry are making great efforts to optimize the recycling process,[6,7] while also reducing the cost and increasing the yield simultaneously.[8] When mass production is realized in the near term, it is believed the cost can be further minimized, and the yield can be maximized. Above all, the electrochemical performance plays a decisive role in whether recycled materials could make a significant impact. Due to the complex

Context & scale

Due to the rapid growth of the demand for lithium-ion batteries, a significant amount of spent lithium-ion batteries is generated every year. Therefore, concerns about resource constraints and environmental issues have been raised. As properly handling spent batteries is urgent and necessary, recycling spent lithium-ion batteries has attracted a lot of attention in both academia and industries. However, although many studies claim that recycled materials have comparable electrochemical performance as commercial materials, industries still doubt it because of the lack of reliable test results. Here, we developed recycled $LiNi_{1/3}Mn_{1/3}Co_{1/3}O_2$ with a unique microstructure, which has the best rate and cycle performance with reliable industrial relevant testing. Thus, this work proves that recycled materials could potentially be reused in new batteries and the profitable recycling process could be realized, and it builds a bridge between academia and industry.

composition of LIBs, impurities will possibly be introduced in different recycling processes. Although many recycling methods claim to eliminate the influence of impurities, the presence of impurities makes people inevitably doubt the performance of recycled materials. Therefore, the verification of performance is critical, and must be fulfilled by trustworthy testing. Since most of the recycling research of lithium-ion batteries is still conducted at lab scale, the testing results are usually associated with coin cells.[9–16] Meanwhile, both the electrode loading (less than 0.62 mAh/cm^2) and active material composition (~80 wt %) in academia are much lower than the industry standard (~3 mAh/cm^2 and ~95 wt % tested in multi-layer pouch cells). Industry has less confidence in recycled materials only from coin cell results. Therefore, from the perspective of electrochemical performance verification of recycled battery materials, long-time and reliable testing needs to be conducted at form factors beyond coin cell. Also, side-by-side comparison with state-of-the-art commercial control materials is essential to deliver competitive benchmarking.

To overcome the challenges mentioned above, we have developed a closed-loop LIBs recycling process that combines the benefits of hydrometallurgical and direct recycling technologies[5,17–24] and can be successfully scaled up.[5,21,24] Here, we demonstrate that recycled cathode materials with optimized microstructure have the best industrial relevant testing results (up to 11 Ah cells) so far and compare them with state-of-the-art commercial equivalent (hereinafter referred to as control). Interestingly, the recycled materials not only pass all the aggressive industrial plug-in hybrid electric vehicle (PHEV) battery tests but also outperform control counterparts in some tests. Through detailed experimental and modeling analysis of pristine and cycled materials, we discover that the unique porous and larger inside void microstructure enables the superior rate and cycle performance and less phase transformation. Compared with the control sample, the surface area of the recycled $LiNi_{1/3}Mn_{1/3}Co_{1/3}O_2$ (NMC111) is 82.14% larger and the cumulative pore volume is 61.25% larger. Even some recycled particles have an outer diameter of the void space equal to 40% to 60% of the particle diameter. The unique microstructure can reduce 16% hoop stress during the discharge/charge process compared with control materials and improve the lithium chemical diffusion coefficient, enabling the superior performance of cycle life and rate performance and less phase transformation. The results pave the way to reintroduce recycled materials into new batteries.

RESULTS

Characterization of pristine materials

Prior to the construction of cells, the pristine recycled and control cathode powder are assessed. As shown in Table S1, the control powder has a composition of $Li_{1.01}Ni_{0.34}Mn_{0.32}Co_{0.34}O_2$, and the recycled powder is $Li_{1.03}Ni_{0.34}Mn_{0.33}Co_{0.33}O_2$, and the impurity in both samples is not detected. As shown in Table S2, recycled materials have a lower tap density, higher surface area, and larger cumulative pore volume, while maintaining a similar particle size compared with control materials. From scanning electron microscopy (SEM) observations (Figure 1A), it is seen that recycled materials possess a similar morphology of primary particles and secondary particles as control materials. It is interesting to note that recycled materials have a larger pore in the center of the particles than that of control materials (Figure S1),[25] which can buffer the strain and deformation to mitigate capacity fading during cycling.[26] The X-ray diffraction (XRD) pattern and its refinement results of recycled powders perfectly match control powders providing good crystallinity (Figure 1B; Table S3). Compared with control powders, recycled powders have a lower degree of

[1]Department of Mechanical Engineering, Worcester Polytechnic Institute, 100 Institute Rd., Worcester, MA 01609, USA

[2]A123 Systems Advanced and Applied Research Center, 200 West St, Waltham, MA 02451, USA

[3]Battery Resourcers, 54 Rockdale St, Worcester, MA 01606, USA

[4]Center for Nanoscale Materials, Argonne National Laboratory, 9700 S Cass Ave, Lemont, IL 60439, USA

[5]Chemical Science & Engineering, Argonne National Laboratory, 9700 S Cass Ave, Lemont, IL 60439, USA

[6]Department of Materials Science and NanoEngineering, Rice University, 6100 Main Street, Houston, TX 77005, USA

[7]National Synchrotron Light Source II, Brookhaven National Laboratory, Upton, NY 11973, USA

[8]United States Advanced Battery Consortium (USABC), 1000 Town Center Drive, Southfield, MI 48075, USA

[9]These authors contributed equally

[10]Lead contact

*Correspondence: yanwang@wpi.edu

https://doi.org/10.1016/j.joule.2021.09.005

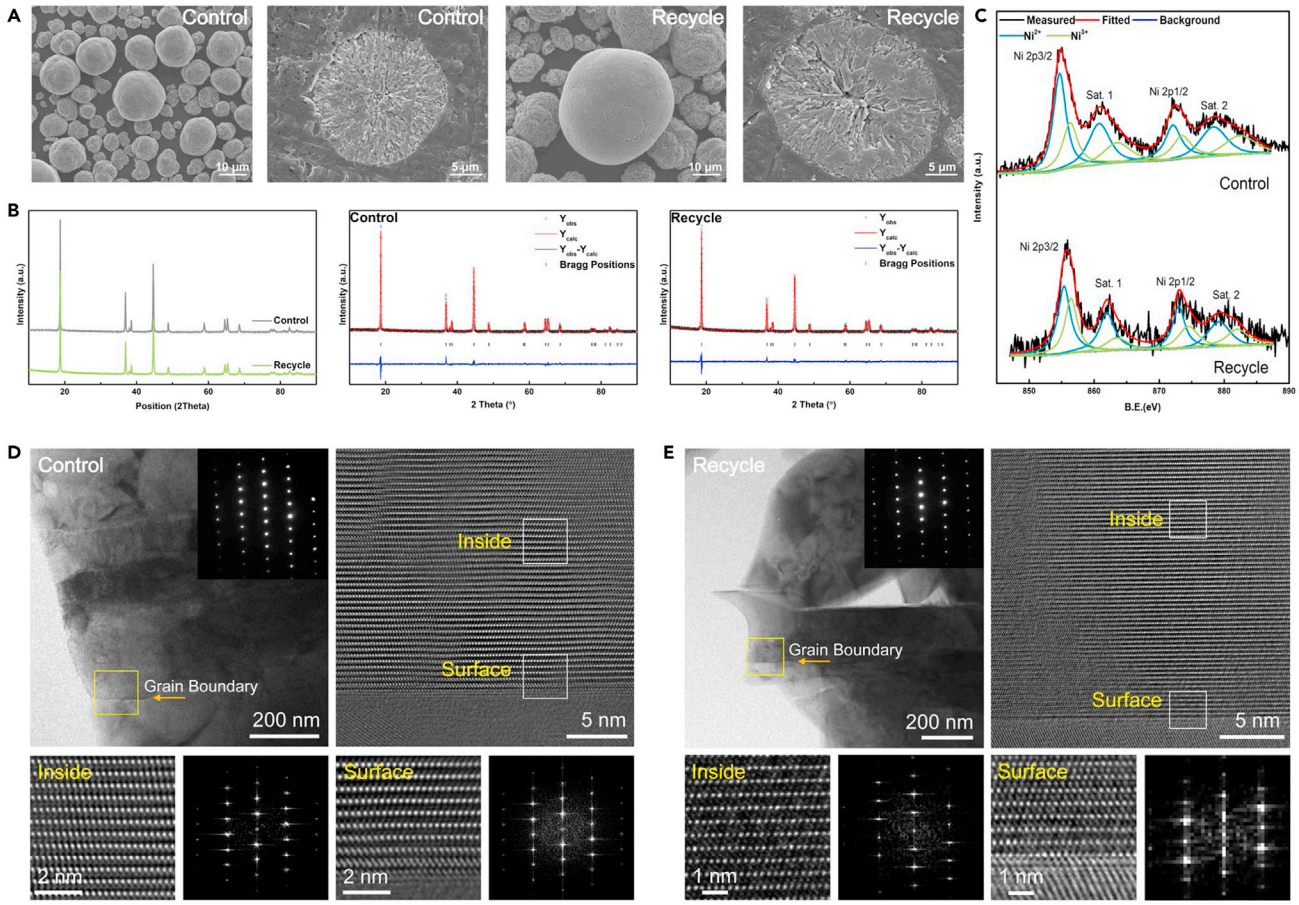

Figure 1. Morphology and crystallinity of control and recycled cathode materials

(A) SEM images and cross-sectional images of control materials and recycled materials.

(B) XRD pattern and Rietveld-refined XRD pattern of control and recycled NMC111.

(C) XPS spectra of Ni 2p of the control and recycle powder.

(D) HRTEM and SAED pattern of pristine control powder. (E) HRTEM and SAED pattern of pristine recycled powder.

Li^+/Ni^{2+} cation mixing, based on the intensity ratio of the (003) and (104) reflections. The X-ray photoelectron spectroscopy (XPS) of Ni 2p (Figure 1C) of the recycled powder shows a peak shift of Ni 2p2/3 to the lower binding energy compared with the pristine control powder. The percentage of Ni^{2+} is 56.34% in the pristine recycled sample and 62.81% in the pristine control sample, indicating a lower Ni^{2+}/Ni^{3+} ratio on the surface of the recycled powder. Due to the similar ionic radii of Ni^{2+} and Li^+, a lower Ni^{2+} content will lead to a lower degree of cation mixing.[27] The XPS spectra of Co 2p and Mn 2p (Figure S2) show that Co^{3+} and Mn^{4+} are dominant in both control and recycled powders. To avoid the surface structure changes caused by sample preparation, the high-resolution transmission electron microscopy (HRTEM) images were taken at the grain boundary inside the particles (Figures 1D and 1E). The selected area electron diffraction (SAED) patterns indicate both bulk materials are layered structures before cycling. The HRTEM images show a decrease in the cation antisite mixing from the surface to the bulk. To confirm the mechanical performance, nanoindentation is employed (Figure S3). Due to the comparable diameters of control and recycled powders, the critical failure compression measurements were comparable across the two particulate systems. Although control powders can resist slightly more compressive pressure than that of recycle powders,

recycled powders are able to withstand ~2 times greater compressive strains prior to critical failure than that of control powders, which means that control powders are more brittle than recycled powders (Figure S3A). The red circles in Figure S3A indicate the significant change in slope, which means that under a lower compressive load, cracks will appear in control samples. The greater elastic modulus for control powders than that of recycled powders (Figure S3B) is consistent with the relative brittle nature of the control granules versus the strain-accommodating recycled materials. In other words, recycled powders can crack later than control powders during repetitive deformation of the charging/discharging process.

Industry-level electrochemical evaluation

To provide evidence that recycled materials can compete with commercial control materials and have practical usage in industry, a top-tier commercial control powder is adopted for side-by-side comparison. Both the recycled powder and control powder are assembled in various cell formats, including coin cells, single-layer pouch (SLP) cells, 1 Ah cells, and 11 Ah cells, and undergo corresponding series tests. All the testing follows the United States Advanced Battery Consortium (USABC) PHEV protocol.[28]

Self-discharge is a parameter to be considered when the car is left idle for a while. On average, the recycled materials lose 5.60 $\pm$ 1.33 mAh/day compared with 7.79 $\pm$ 0.20 mAh/day of the control material in a 7-day interval test. The actual discharge capacity is also determined (0.980 $\pm$ 0.013 Ah for recycled materials and 0.991 $\pm$ 0.007 Ah for control materials). The volumetric energy density of 1Ah pouch cell with recycled materials is 344.43 Wh/L, which is slightly smaller than 348.29 Wh/L of 1Ah pouch cell with control materials. The gravimetric energy density of 1Ah pouch cell with recycled materials is 140.22 Wh/kg, similar to 141.80 Wh/kg of 1Ah pouch cell with control materials. Because the electrode preparation targets the same loading and press density, there is a very minor difference between the volumetric and gravimetric energy density of recycled and control materials.

The cold crank test simulates that vehicles are in an extremely cold environment and tends to measure the voltage threshold of the battery at -30°C and state of charge (SOC) accordingly. As shown in Figure 2A, at -30°C, recycled and control materials can sustain above 2.2V voltage limit after three consecutive discharge pulses (2.33W). The resistances of recycled and control cells are demonstrated by the hybrid pulse power characterization (HPPC) test corresponding reference performance test (RPT) and SOC in Figure 2B. The discharge resistance of HPPC test shares a similar trend among all test samples. As the depth of discharge (DOD) progresses, resistance fluctuates slightly and suddenly increases significantly when SOC is approaching 0%. Generally, the recycled powder shows a slightly higher resistance than the control powder. At 50% SOC, the resistance increase from RPT0 to RPT13 is basically the same for recycled materials (29.32%) and control materials (28.35%).

Calendar life mimics a minimal usage of battery and establishes the degradation rate at 50°C to accelerate the decay process. Figure 2C depicts that after 384 calendar days, recycled powder maintains 88.43% capacity retention, whereas control powder has 86.89% retention.

Figure 2D shows the cycle performance of 1Ah cells with recycled NMC111 and control NMC111. The end of life and end of testing requirements were set at 80% and 70%, respectively. Here, the recycled materials show a prominent advantage

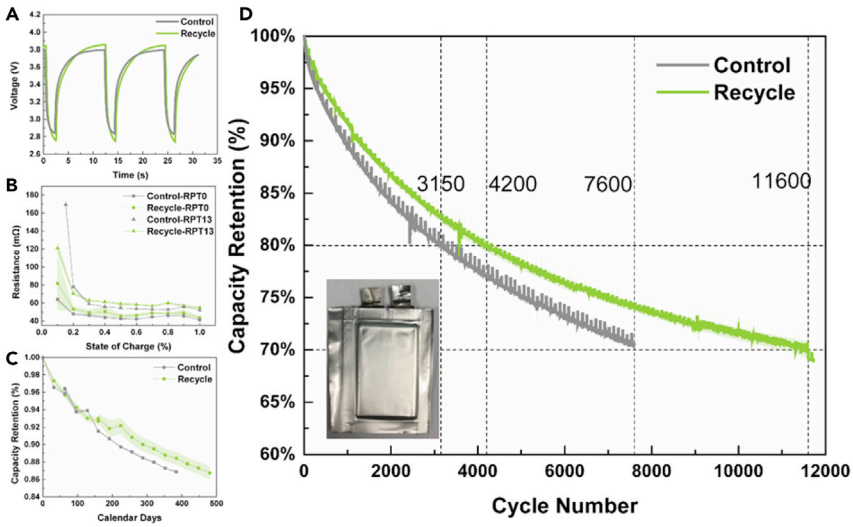

Figure 2. 1Ah cell evaluation of control powder (in gray) versus recycled powder (in green)

(A) Cold crank test.

(B) HPPC-resistance at RPT0 and RPT 13.

(C) Calendar life testing at 50°C.

(D) Cycle life testing at 45°C between 2.7–4.15 V with each cycle of 1C charge and 2C discharge where solid line is the average capacity retention and the shaded area is the corresponding error bar; the insert figure located in the lower-left region demonstrates the actual fabricated 1Ah cell.

compared with the control powder, with the degradation rate being much slower. The recycled materials have a cycle life of 4,200 cycles before reaching to 80% capacity retention and an astonishing 11,600 cycles to 70% capacity retention. Under the same conditions, the control materials accrued 3,150 cycles to 80% capacity retention and 7,600 cycles to 70% capacity retention. This result indicates the cycle life can be improved by 33% to 53% with the recycled powder depending on the set point of end of life. To our knowledge, the 11,600 cycles is the best cycling result observed from recycled materials evaluations so far, and it is reached at multi-layer 1 Ah cells with harsh industrial-level testing.

Coin cells, SLP (Figure S4), and industry-level 11 Ah (Figures S5 and S6) cells are also built to benchmark the recycled powder and compared it with control powder. The physical characterization of SLP and 11 Ah cells has been tested (Figure S7; Table S4). In summary, all format cells with recycled materials pass all rigorous industry-level tests and show a comparable capacity with control materials at a low rate. In coin cells, recycled materials show 88% to 170% higher capacity than control materials at 5C. SLP cells with recycled materials have a 25% better cycle life than that with control materials. In addition, it is very impressive that compared with the 1C discharge capacity, the recycled 11 Ah cell maintains over 60% at 5C and approaching 30% at 9C, which significantly exceeds the control 11 Ah cell (~48% at 5C and ~17% at 9C). The recycled powder has a better diffusivity than the control powder during charging and has the similar diffusivity as the control powder during discharge (Figure S8). Thus, the resulting outcome shows that recycled materials can meet or exceed the industry standards. It can further clear any hesitation of employing recycled cathode powder in commercial cells.

Teardown analysis for cycled control and recycled electrodes

Aiming to understand why the recycled powder has much better cycle life and rate performance compared with control powder, 1Ah cells with both recycled and

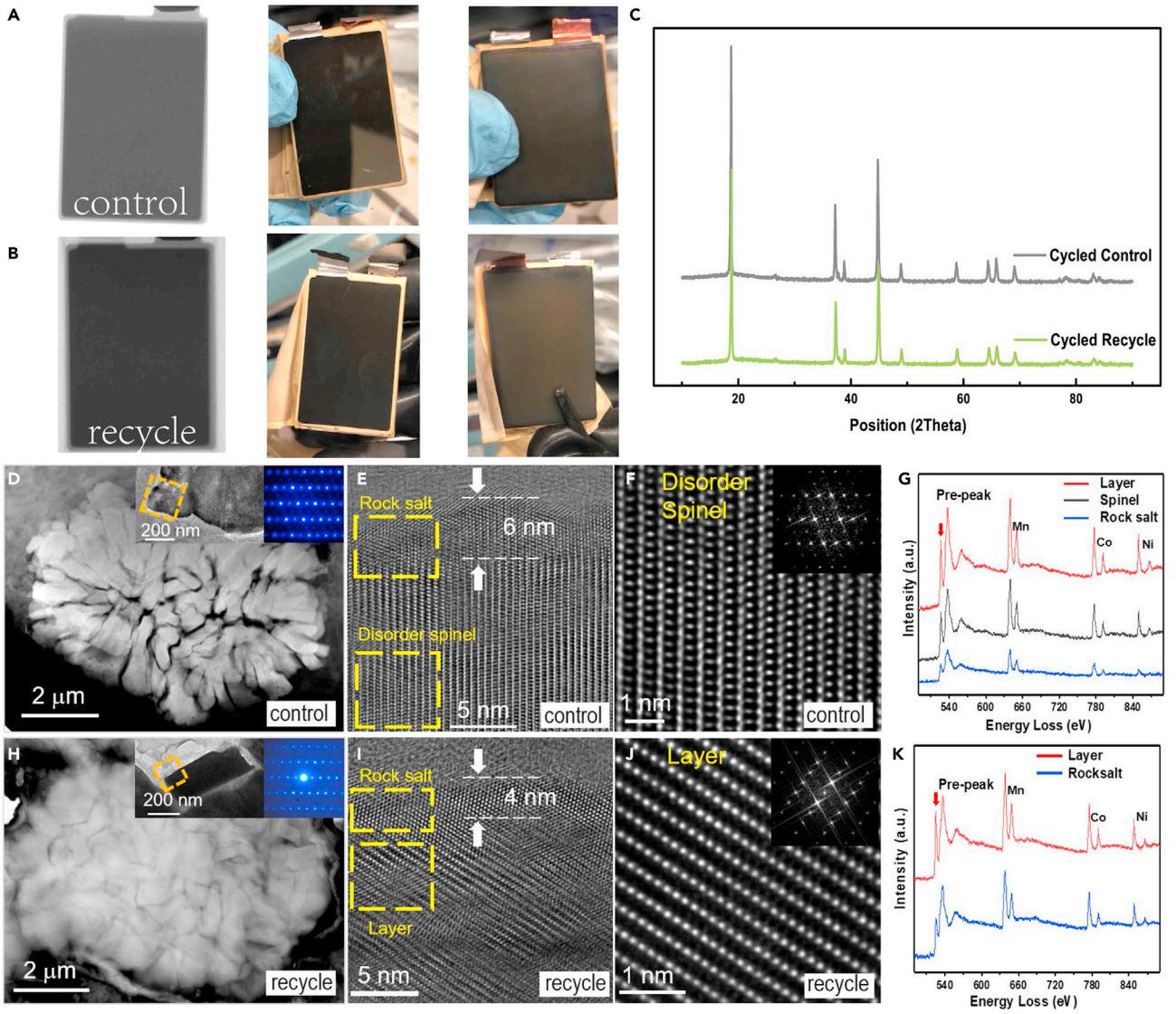

Figure 3. Teardown analysis and comparison between cycled recycled and control cathodes

(A) X-ray images of cycled control cell, Teardown pictures of cycled control cathode and anode.

(B) X-ray images of cycled recycle cell, Teardown pictures of cycled recycle cathode and anode.

(C) XRD of cycled control and recycle electrode.

(D) High-angle annular dark-field (HAADF) image of the control sample after cycling to 70% SOC, the insert shows HRTEM image of the cycled control sample and corresponding SAED pattern showing a mixture of layered and spinel structure.

(E) High-magnification TEM image showing rock-salt structure at surface followed by disordered spinel for the cycled control sample.

(F) HRTEM image showing disordered spinel structure inside the cycled control sample.

(G) EELS spectra from three areas in (E).

(H) HAADF images of recycled sample after cycling to 70% SOC, the insert shows HRTEM of the control sample and corresponding SAED pattern showing a mixture of layered and spinel structure.

(I) High-magnification TEM image showing rock-salt structure at surface for the cycled recycled sample.

(J) HRTEM image showing perfect layered structure inside the cycled recycled sample.

(K) EELS spectra from two areas in (I).

control powders were disassembled. X-Ray and visual images of cycled electrodes are shown in Figures 3A and 3B. It is worth mentioning that the cells are wet with electrolyte, and the drying-out effects of electrolytes can be excluded. Both control and recycled cells have intact cell structures, and no electrode or tab damage is

detected. Additionally, through X-ray probing, the alignment between electrodes is still unchanged. This validates that cycling or rate performance differences are not caused by any cell construction variations or cell damage during tests, and it also highlights the high manufacturing quality and integrity of cells tested under such aggressive testing conditions. Then, cycled electrodes undergo capacity evaluation, and the results are shown in Table S5. The control cathode has a slightly higher discharge capacity than that of the recycle cathode, because of shorter cycles of the control cathode.

XRD pattern comparison of cycled electrodes is shown in Figure 3C. XRD refinement results are shown and listed in Figure S9 and Table S6. The lattice parameter *a* shrinks and the lattice parameter *c* expands after cycling for both control powder and recycled powder.[29] Two dominant factors lead to the expansion in c axis and shrinkage in a axis. As lithium ions deintercalate from the Li layer, the increased repulsion of the oxygen layer results in the expansion along the c axis because the screening effect is diminished during delithiation. Meanwhile, due to the increased oxidation state of the transition metal oxide, their ionic radius is decreased, which contributes to the shrinkage along a axis.[26,30] Here, we find recycled powders have a similar deviation in the a axis direction (0.53% shrinkage) and a smaller deviation in the c axis direction (0.84% expansion) between uncycled and cycled powder compared with control powder (a axis, 0.54% shrinkage; c axis, 0.91% expansion). The greater change in the c axis direction will lead to larger distortion, which will exert greater pressure on adjacent primary particles, resulting in the cracks during cycling.

To further understand the degradation mechanism, transmission electron microscopy (TEM) is employed to directly observe the microstructural changes. The recycled sample has fewer cracks after cycling to 70% SOC in Figures 3D, 3H, and S10, showing better mechanical properties.[31–34] The SAED pattern in Figure 3H demonstrates that the recycled bulk material retains the layered structure after 11,600 cycles. In contrast, the control sample shows a mix of layered and spinel structure after 7,600 cycles (Figure 3D). For the recycled sample, HRTEM image clearly shows that a rock-salt structure about 4 nm thick is formed on the surface, whereas the bulk of the particle retains the highly ordered layered structure (Figure 3I).[35] The intensity profile of transition metals (TMs) in Li layer indicated by the orange arrow shows that the TM cations are more mixed at the surface compared with the inside (Figure S11). In comparison, the microstructure of the control sample exhibits more significant changes after cycling. The surface turns into the rock-salt phase (~6 nm thick from the surface) in Figure 3E, which is thicker than the recycled sample. Even more so, the bulk of the particle experienced structural collapse and displays a disorder spinel phase. This collapsed region extends ~40 nm into the bulk of the grain (Figure S12). The electron energy-loss spectroscopy (EELS) spectra (Figures 3G and 3K) are analyzed in different phase areas to investigate the structural reconstruction. It is found that the valence of Co and Ni remains almost unchanged in both samples. The Mn-L edge spectra in the control sample has a larger difference of the L3/L2 ratio between the surface and bulk, indicating that more Mn is dissolved in the electrolyte, which causes the slight decrease of its valence state at the surface.[36,37] The energy dispersive X-ray spectroscopy (EDS) linear scan (Figure S13) further confirms the dissolution of more Mn in the control sample, which will result in the unequal pressure distribution in the particles, accelerating the cracking and capacity fading.[38] The thickness of the cathode electrolyte interface (CEI) layer and the segregation of TMs are also investigated via TEM. The thickness of CEI layer is determined via F detection on the surface (Figure S14). Due to undergoing longer

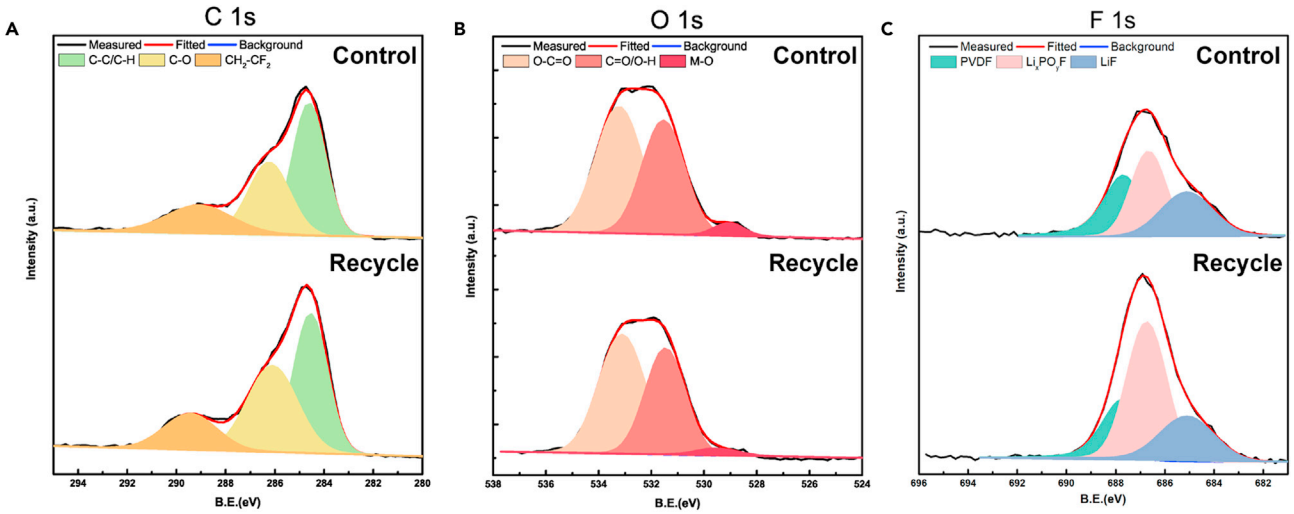

Figure 4. CEI layer comparison between cycled control and recycled electrodes

(A–C) XPS of C1s (A), O1s (B), and F1s (C) of the cycled control and recycled electrodes.

cycles, the thickness of the CEI layer of recycled particles (~200 nm) is thicker than that of control particles (~100 nm), which is consistent with the XPS results (Figure 4). XPS measurements are used to investigate differences of CEI between the control and recycled cathode after cycling to 70% SOC. The C 1s and O 1s spectrum of both cathodes (Figures 4A and 4B) show similar intensity profiles, indicating similar degradation of the electrolyte after prolonged cycling. The O 1s spectra of the cycled control cathode displays a peak at ~529.3 eV, corresponding to M-O bonding from NMC, and has a higher intensity than that of the cycled recycled cathode, indicating a thinner CEI layer of control electrode. The peak at ~687.7 eV is CF_2 in Figure 4C, which formed more at the surface of cycled control cathode (36.77%) compared with cycled recycled cathode (26.12%). In XPS, CF_2 is solely from polyvinylidene fluoride (PVDF) binder present under the CEI layer. The CF_2 intensity decreases as the CEI gets thicker as the CEI blocks the signal from PVDF. Thus, it can be estimated that strong CF_2 intensity refers thin CEI layer, which further indicates that cycled control cathode has a thinner CEI layer. In conclusion, although the recycled sample is cycled 4,000 cycles more than the control sample, it still shows less phase change and segregation of the TMs, resulting in superior mechanical properties, which delays cracking and fracturing, inhibiting the degree of side reactions between the electrolyte and newly exposed surfaces.

Modeling

To further probe the structural difference between the recycled and control samples, we performed full-field transmission X-ray microscopy[39–41] on both types of pristine particles with nanotomography and reconstructed their 3D structures with a spatial resolution of 40 nm. Consistent with the SEM observations, Figure 5A shows that the recycled particles have a significant fraction of internal pore volume, whereas the control samples have a much more compact structure (Figure 5B). Furthermore, the tomographic images reveal that the internal pore space in the recycled sample exists in two forms, i.e., disconnected micro-pores distributed within the particles and irregularly shaped, interconnected void space located at the particle center, see Figure 5C, which results from the synthesis process. Measurement of several particles shows that the outer diameter of the void space amounts to 40% to 60% of the particle diameter. The particles in the control sample also frequently have central

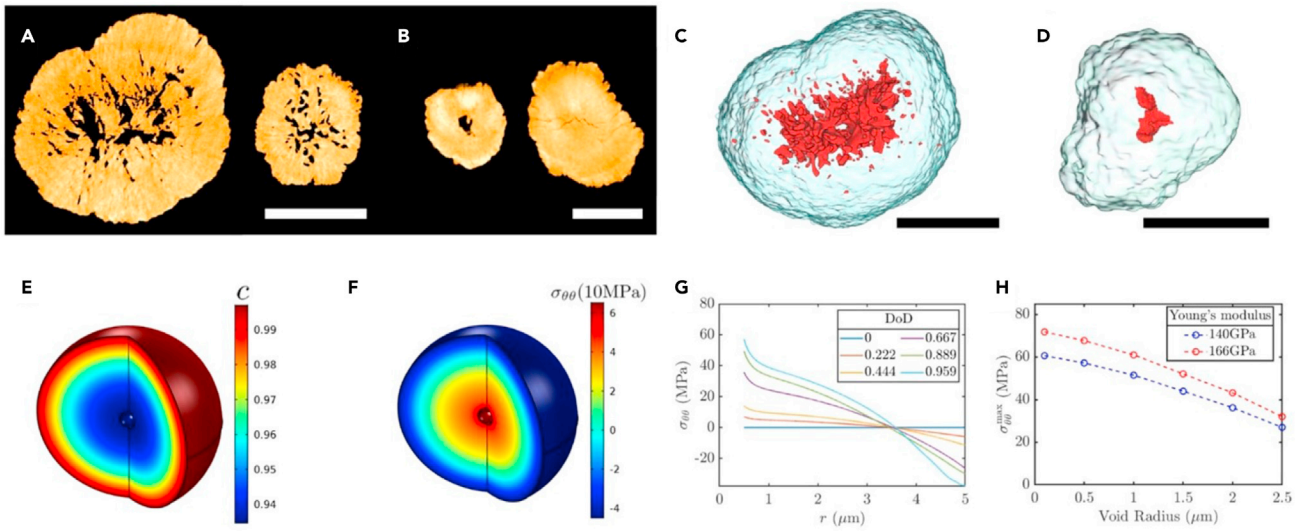

Figure 5. Nanotomography and complementary modeling of the microstructure

(A and B) Examples of NMC111 particle cross sections from (A) the recycled sample and (B) the control sample.

(C and D) Visualization of the internal void (red) in an NMC111 secondary particle from the recycled and control samples, respectively. Distributed small pores with volume less than 0.001 μm3 are removed from the particle for the ease of viewing. Scale bar, 10 μm in (A) and (C) and 5 μm in (B) and (D).

(E and F) Lithium concentration c (E) and hoop stress $\boldsymbol{\sigma_{\theta\theta}}$ (F) distributions in a 10 μm particle with a 1 μm void, which is discharged to DOD = 95.3% at 2C.

(G) Evolution of $\boldsymbol{\sigma_{\theta\theta}}$ in the radial direction with DOD.

(H) Maximum hoop stress $\boldsymbol{\sigma_{\theta\theta}^{max}}$ at the void surface during 2C discharge versus void radius. The blue and red lines represent $\boldsymbol{\sigma_{\theta\theta}^{max}}$ calculated using a Young's modulus of 140 GPa (recycled sample) and 166 GPa (control sample), respectively.

voids but with a much smaller size (Figure 5D). Through modeling described further on, we find that both types of pores contribute to a reduced stress level during the discharge/charge process. Although small, distributed pores lower the effective elastic moduli of the NMC111 particles, and the large voids decrease the stress concentration at the inner pore surface.

We simulated the galvanostatic discharge/charge process in a single NMC111 particle with a void inside, which is approximated as a spherical pore to simplify calculation. The simulation couples the lithium diffusion with solid mechanics to predict the stress distribution within the particle, see details in experimental procedures. Figure 5E and 5F show the distributions of the lithium concentration and hoop stress ($\sigma_{\theta\theta}$), respectively, in a 10 μm particle with a 1 μm void when it is discharged at 2C to a DOD of 95.3%. A small Li concentration gradient is present in the radial direction. Nevertheless, the non-uniform lattice expansion induced by the gradient generates a significant tensile hoop stress (58 MPa) at the internal void surface, which makes the particle prone to crack nucleation from inside as observed in experiment. A stress gradient of similar magnitude develops upon charging, but the stress becomes compressive at the inner surface. Figure 5G shows the radial distribution of $\sigma_{\theta\theta}$ at different DODs upon discharging. It can be seen that $\sigma_{\theta\theta}$ rises rapidly with DOD especially near the void surface. The maximum tensile hoop stress $\sigma_{\theta\theta}^{max}$, however, decreases with the void size. As illustrated in Figure 5H, $\sigma_{\theta\theta}^{max}$ is lowered by 55% when the void radius increases from 100 nm to 2.5 μm, showing that larger voids can more effectively accommodate the Li-insertion-induced volume change to alleviate stress concentration. Furthermore, the lower Young's modulus (140 GPa) of the more porous recycled particles causes $\sigma_{\theta\theta}^{max}$ to be 16% smaller than in the control particles with the same-sized void (red dashed line in Figure 5H), which has a larger stiffness of 166 GPa. Therefore, both the distributed pores and large void in the recycled

NMC111 particles play a beneficial role in decreasing the tensile stress at the inner particle surface, which reduces the likelihood of crack initiation and growth and contributes to their extended cycle life.

DISCUSSION

In summary, we show the best results of recycled materials reported with long term and reliable testing in the rigorous industrial-level tests. According to the detailed experimental analysis and modeling results, recycled materials have an optimized microstructure of larger surface area, cumulative pore volume, and larger inside void, which provide higher Li chemical diffusion coefficient and mitigate the strain during cycling, and this leads to less phase transformation and benefits superior performance. Impressively, the 1 Ah cells of recycled NMC111 have a lifetime of 11,600 cycles, whereas control equivalent cannot surpass 7,600 cycles when reaching to the end of life (70% capacity retention). Through this trustworthy testing and thorough comparison, it becomes clear that recycled materials can be as good as or even better than the high-quality control materials. We envision that recycled cathode materials could be a potentially viable and competitive product to be adopted in current battery manufacturing process, leading to a sustainable Li-ion battery manufacturing ecosystem.

EXPERIMENTAL PROCEDURES

Resource availability

Lead contact

Further information and requests for resources should be directed to and will be fulfilled by the lead contact, Yan Wang (yanwang@wpi.edu).

Materials availability

This study did not generate new unique reagents.

Data and code availability

This study did not generate any datasets.

Recycling process

In the recycling process (Figure S15), 30 kg spent LIBs of any type and state can be combined into a single feedstock. Spent batteries are first discharged to less than 2 V via a resistor to avoid unintended thermal runaway during processing. The discharged batteries are then cut, shredded, and sieved. The steel cases, current collectors (Al and Cu), electronics circuits, plastics, and pouch materials are removed and recycled. The remaining black mass consists of graphite, carbon, cathode material, and some residues of Al, Cu, and Fe. After that, a hydrometallurgical process is implemented, and different cathode materials and metals are dissolved in the leaching solution. Meanwhile, graphite, carbon, and undissolved materials are filtered out. First, impurities in the leachate, including Cu, Fe, and Al are removed through a series of pH adjustments, leaving Ni, Mn and Co ions. The content of Ni, Mn, Co and impurities varies with different feeding stocks. Table S7 reveals the ICP-OES results for leaching and purified solution of one of the batches. The leaching solution contains some impurities, including Cu, Fe, and Al. After the impurity removal step, impurities are significantly removed. In addition, the concentration of Na increases because of adding NaOH to control the pH for impurity removal. And the concentration of Ni, Mn, Co, and Li decreases because of the volume change after the impurity removal step. The recovery rate of Ni, Mn, and Co are over 90%. Next, the ratio of Ni, Mn, and Co is tailored to the desired ratio by adding virgin metal sulfates as needed. The ability to fabricate various $LiNi_xMn_yCo_{(1-x-y)}O_2$ (NMC) (responding to market

demand) is a key advantage of this recycling technology versus competing processes. Subsequently, the adjusted metal sulfate solution undergoes the co-precipitation reaction under nitrogen, and the pH value is controlled between 10–11 to produce transition metal hydroxide precursor powder. Then, 1 mol of the precursor is mixed with 1.05 mol of lithium carbonate. Finally, the mixture is sintered at 450°C for 5 h and 900°C for 14 h. After calcination, recovered NMC cathode power is ready for use in "new" batteries, enabling a closed-loop approach for the cathode materials. The recycled materials are then evaluated in various cell formats (coin cell, SLP, 1 Ah cell, and 11 Ah cell) and compared with commercially equivalent side-by-side.

Here, the growth process of precursor particles during co-precipitation reaction is revealed in Figure S16. In the early stage, the particles are uniform and less densely packed. As the reaction continues, existing particles grow larger and denser, while new nucleates form. Due to the thermodynamic and kinetic reasons, a limiting size for precursor particles and particles will not grow anymore when it hits this limit. As we can imagine, after a specific time, the distribution of three particles (largest particle, nucleates, and growing particle) will become unchanged and the reaction reaches its steady status. In the demonstration of Figure S16, this steady state is reached after 3 days, and the associated tap densities can also verify this statement.

Materials characterization

SEM (JEOL JSM 7000 F) were employed to obtain information of particle size and particle morphology. The phase structures of the pristine and cycled materials were identified by XRD (PANalytical Empyrean Series 2 X-ray diffraction System) with Cu Kα radiation (45 kV, 40 mA). FullProf Suite software was utilized to obtain structural parameters of pristine and cycled materials. Inductively coupled plasma optical emission spectrometry (Perkin Elmer Optima 8000 ICP-OES) was used to obtain the concentration of metal ions in materials. Tap density measurements were acquired by 1,800 taps on a STAV 2003 Stampf volumeter. Particle size distribution was obtained using a Malvern Mastersizer 3000. Surface area results were determined using a Micromeritics TriStar II analyzer. Mechanical property evaluation of individual microparticles was performed by nanoindentation (iMicro Pro, Nanomechanics) with an InForce 1,000 mN actuator and a 75 μm diameter flat-punch diamond nanoindenter tip from Synton-MDP (Switzerland). The HRTEM observation were performed at the Argonne Chromatic Aberration-corrected TEM (ACAT, a FEI Titan 80–300 transmission electron microscope equipped with an image corrector to correct both spherical and chromatic aberrations). EELS was acquired using the ACAT operated at 200 KV in an image-coupled S/TEM mode. High-angle annular dark-field (HAADF) imaging and STEM-EDS mapping was carried out using a scanning transmission electron microscope (STEM) (Thermo Fisher Scientific, Talos F200X). TEM specimen was prepared using Ar^+ ion milling with an accelerating voltage of 4 kV followed by an ion milling polishing process with an accelerating voltage of 0.3 kV. Cycled electrodes were washed with dimethyl carbonate (DMC) to remove any residue electrolyte. Samples after drying were then transferred into XPS chamber without air exposure through an argon-atmosphere glovebox connecting system. XPS analysis was conducted using a PHI 5000 VersaProbe II System (Physical Electronics). The spectra were obtained using Al Kα radiation (hν = 1,486.6 eV) (100 mm^2 area, 25 W), Ar^+, and electron beam sample neutralization in fixed analyzer transmission mode. The high-resolution spectra were acquired at a pass energy of 23.50 eV. The XPS binding energies were calibrated to the carbon black component in the C1s spectra at 284.8 eV. Peak fitting was performed using Shirley

background correction and the Gaussian–Lorentzian curve synthesis available in the XPSPeak 41 software.

Nanotomography was conducted at beamline 18-ID FXI of NSLS-II at Brookhaven National Laboratory with incident X-ray energy fixed at 8.4 keV. The NMC particles were loaded in a Kapton tube, and their projections were collected using a fly scan mode over 180° rotation range. A 2k × 2k CCD camera was used with binning 2 × 2, providing a field of view of 40 × 40 μm and a spatial resolution of 40nm. Nanotomographic images were reconstructed using open-source Python packages PyXAS[42] and TomoPy[43] and visualized in Avizo 9.0.

Cell fabrication and electrochemical testing protocol

Coin cell

The cathode electrodes were fabricated from a 94% mixture of NMC with a balance of conductive carbon and PVDF in N-methyl-2-pyrrolidone (NMP). The slurries were mixed benchtop scale using a Thinky mixer model ARE-310. The slurries were then cast onto aluminum foil using a wet film applicator on a Sheen Automotaic Film Applicator model 1-133N. Electrodes were set to a target loading density of ~18 mg/cm^2 and pressed to 3.0 g/cc. Cells were then constructed in an argon glovebox paired against Li metal. Once constructed, cells were formed at slow rate charge and discharge cycles between 4.3 and 2.7 V and then charged at 0.5 C to 4.3 V and discharged at various C-Rates to 2.7 V at room temperature. Cyclic voltammetry (CV) curves were obtained from an electrochemical analyzer (Bio-Logic SAS VMP3) using the EC-Lab V10.40 program. The testing potential range was between 2.8 V and 4.6 V (versus Li/Li$^+$) at the scan rate of 0.1, 0.4, 0.7, and 1.0 mV/s.

Single-layer pouch cell

The cathode electrodes were fabricated from a 94% mixture of NMC with a balance of conductive carbon and PVDF in NMP. The slurries were mixed benchtop scale using a Thinky mixer model ARE-310. The slurries were then cast onto aluminum foil using a wet film applicator on a Sheen Automotaic Film Applicator model 1-133N. Electrodes were set to a target loading density of 18.5 mg/cm^2. The cathode electrodes were matched with a water-based graphite anode fabricated on A123 systems' R&D coater. SLPs were constructed in a dry room environment and were formed at room temperature, using slow rate charge and discharge cycles and then cycled at 1C Charge/2C Discharge between 4.2V and 2.7V using a Maccor Series 4000 Battery Tester.

1Ah cell

The cathode electrodes were fabricated from a 94% mixture of NMC with a balance of conductive carbon and PVDF in NMP. The slurries were mixed in a dry room environment and coated on A123 systems' R&D coater with target loading density 19.65 mg/cm^2. The cathode electrodes were matched with a water-based graphite anode fabricated on A123 systems' R&D coater. 1Ah cells were constructed in a dry room environment and were formed at room temperature, using slow rate charge and discharge cycles, and then cycled at 45°C 1C Charge/2C Discharge between 4.15 and 2.7 V using a Maccor Series 4000 Battery Tester. During cycle life testing, a state of health (SOH) check is performed every month, which involves a 5C discharge pulse for 20 s at 70%, 50%, and 20% SOC. Cells also underwent two different HPPC protocols at RPT0 and RPT13 (perform RPT every 32 days). Cold crank was tested at 3 fixed power discharge pulses for 2 s with a 10 s rest between pulses at −30°C and 15%SOC. The calendar life was conducted by applying a pulse once per day and then reposing the tested cells under open-circuit voltage (OCV)

monitoring at 50°C. The actual cell capacity was measured from full charge to the discharge voltage limit. Then, the cell was recharged and stood in an open-circuit condition for 7 days. The cell was discharged to 2.7 V for its residual capacity, and recharged and discharged again. The observed loss of capacity is self-discharge capacity.

11Ah cell

The cathode electrodes were fabricated from a 94% mixture of NMC with a balance of conductive carbon and PVDF in NMP. The slurries were mixed with an 8 kg Asada mixer in a dry room environment and coated on A123 systems' pilot coater with target loading density 19.5 mg/cm^2. The cathode electrodes were matched with a water-based graphite anode fabricated on A123 systems' pilot coater. 11Ah cells were constructed in a dry room environment and were formed at room temperature, using slow rate charge and discharge cycles, and then cycled at 45°C 1C Charge/2C Discharge between 4.2 and 2.7 V using a Maccor Series 4000 Battery Tester. Rate performance was tested at (1C/−1C, -2C, −3C, −5C, −7C, −9C) at 25°C from 4.15–2.7 V. Cells also underwent two different HPPC protocols at 25°C (100%SOC to 0%SOC with −5C/+3.75, 30 s) and at 0°C (100%SOC to 0%SOC with −5C/+1.5C, 30s). Cold crank was tested at 3 fixed power discharge pulses for 2 s with a 10 s rest between pulses at −30°C and 15% SOC. Cells were also tested using National Instruments LabVIEW custom software and hardware for control and data acquisition. The calendar life and self-discharge were tested by a similar protocol as 1 Ah cells.

Single particle discharge/charge simulation

A single particle model is used to simulate lithium diffusion and intercalation-induced stress within a void-containing NMC111 particle during the (dis)charging process. Li diffusion is described by the following diffusion equation:

$$\frac{\partial c}{\partial t} = \nabla\cdot\left[\frac{DV_m}{RT}c(1-c)\nabla\mu\right], \qquad \text{(Equation 1)}$$

where c is the Li concentration field normalized by its maximum value C_{max} in NMC111 and μ is the Li chemical potential. The meanings and values of other parameters in Equation 1 are listed in Table S8. We consider both the chemical and stress contributions to μ, which has the expression:

$$\mu = -\frac{F}{V_m}U_{eq}(c) + \frac{\partial f_{el}}{\partial c}, \qquad \text{(Equation 2)}$$

where $U_{eq}(c)$ is the equilibrium potential of NMC111 taken from the previous work,[44] andf_{el} is the elastic energy density

$$f_{el}(\varepsilon_{ij}, c) = \frac{1}{2}C_{ijkl}\left[\varepsilon_{ij} - \varepsilon^0_{ij}(c)\right]\left[\varepsilon_{kl} - \varepsilon^0_{kl}(c)\right] \qquad \text{(Equation 3)}$$

where ε_{ij} is the total strain, $\varepsilon^0_{ij}(c)$ is the stress-free strain tensor that describes the Li-concentration-dependent lattice parameters of NMC111. Because of the polycrystalline nature of NMC secondary particles, $\varepsilon^0_{ij}(c)$ is approximated as isotropic: $\varepsilon^0_{ij}(c) = \delta_{ij}\varepsilon_0(c - c_{min})/(1 - c_{min})$, where ε_0 is the orientation-averaged lattice misfit between the fully discharged and charged (4.15 V) states, c_{min} is the Li concentration at the fully charged state and δ_{ij} is the Kronecker delta tensor. The stiffness tensor C_{ijkl} is also assumed to be isotropic and expressed by the Young's modulus E and Poisson ratio ν. A zero Li flux boundary condition is applied to the void surface inside the particle, and the Li flux at the outer particle surface obeys the Butler-Volmer kinetics

$$j_{in} = V_m k_0 C_l^{1-\alpha} C_{max}^{2\alpha} c^{\alpha} (1-c)^{\alpha} \left\{ \exp\left[-\frac{(1-\alpha)(\mu - \mu_{el})V_m}{RT} \right] - \exp\left[\frac{\alpha(\mu - \mu_{el})V_m}{RT} \right] \right\},$$

(Equation 4)

where μ_{el} is the Li chemical potential in the electrolyte, which is varied in simulation to maintain a constant total Li flux specified by the (dis)charge rate. The diffusion equation is solved in conjunction with the linear elasticity equation with traction-free boundary condition at the particle surface to determine the evolution of the Li concentration and stress fields. Consistent with the experiment, the discharge or charge simulation is started or terminated at 4.15 V, respectively. The lower cutoff voltage is 3.5 V. The model is solved by the finite-element method implemented in COMSOL Multiphysics 5.3a assuming the system to be 2D axisymmetric.

SUPPLEMENTAL INFORMATION

Supplemental information can be found online at https://doi.org/10.1016/j.joule.2021.09.005.

ACKNOWLEDGMENTS

This material is based upon work supported by the Department of Energy, National Energy Technology Laboratory under award number DE-EE0006250 with the United States Advanced Battery Consortium LLC (USABC LLC). Y.Z. is supported by NSF CMMI-1929949. F.W. and M.T. acknowledge support from DOE under project no. DE-SC0019111. Simulations were partially performed on supercomputers at the Texas Advanced Computing Center (TACC) at the University of Texas. This research used resources of the FXI beamline (18-ID) of the National Synchrotron Light Source II, a User Facility operated for the DOE Office of Science by Brookhaven National Laboratory under contract no. DE-SC0012704. Use of the Center for Nanoscale Materials, an Office of Science user facility, was supported by the U.S. Department of Energy, Office of Science, Office of Basic Energy Sciences, under contract no. DE-AC02-06CH11357. Work carried out at Post Test Facility of Argonne National Laboratory, operated for DOE Office of Science by UChicago Argonne, LLC, under contract no. DE-AC02-06CH11357.

AUTHOR CONTRIBUTIONS

Conceptualization, Y.W.; methodology, M.C., Z.Z., and X.M.; investigation, X.M., M.C., Z.Z., D.B., J.W., C.H., E.G., Y.L., Z.Y., Y.Z., F.W., D.R., S.S., I.B., J.W., M.G., X.X., W.-K.L., M.T., Q.W., J.F., Y.Z., and B.S.; visualization, X.M., M.C., D.B., Y.L., Z.Y., Y.Z., and F.W.; funding acquisition, Y.W.; project administration, Y.W., R.A., P.K., and N.S.; supervision, Y.W., R.A., P.K., and N.S.; writing – original draft, X.M., M.C., and M.T.; writing – review & editing, X.M., Y.W., M.C., Z.Z., D.B., J.W., C.H., E.G., Y.L., Z.Y., Y.Z., F.W., D.R., S.S., I.B., J.W., M.G., X.X., W.-K.L., M.T., Q.W., J.F., Y.Z., B.S., R.A., P.K., and N.S.

DECLARATION OF INTERESTS

Y.W. is a co-founder and Chief Scientist of Battery Resourcers, which is developing a lithium-ion battery recycling process. There is a patent application based on the research results reported in this paper.

Received: May 15, 2021
Revised: August 3, 2021
Accepted: September 16, 2021
Published: October 14, 2021

REFERENCES

1. Harper, G., Sommerville, R., Kendrick, E., Driscoll, L., Slater, P., Stolkin, R., Walton, A., Christensen, P., Heidrich, O., Lambert, S., et al. (2019). Recycling lithium-ion batteries from electric vehicles. Nature *575*, 75–86. https://doi.org/10.1038/s41586-019-1682-5.

2. Ciez, R.E., and Whitacre, J.F. (2019). Examining different recycling processes for lithium-ion batteries. Nat. Sustain *2*, 148–156. https://doi.org/10.1038/s41893-019-0222-5.

3. Fan, X., Hu, G., Zhang, B., Ou, X., Zhang, J., Zhao, W., Jia, H., Zou, L., Li, P., and Yang, Y. (2020). Crack-free single-crystalline Ni-rich layered NCM cathode enable superior cycling performance of lithium-ion batteries. Nano Energy *70*. https://doi.org/10.1016/j.nanoen.2020.104450.

4. Or, T., Gourley, S.W.D., Kaliyappan, K., Yu, A., and Chen, Z. (2020). Recycling of mixed cathode lithium-ion batteries for electric vehicles: current status and future outlook. Carbon Energy *2*, 6–43. https://doi.org/10.1002/cey2.29.

5. Chen, M., Ma, X., Chen, B., Arsenault, R., Karlson, P., Simon, N., and Wang, Y. (2019). Recycling end-of-life electric vehicle lithium-ion batteries. Joule *3*, 2622–2646. https://doi.org/10.1016/j.joule.2019.09.014.

6. Lv, W., Wang, Z., Cao, H., Sun, Y., Zhang, Y., and Sun, Z. (2018). A critical review and analysis on the recycling of spent lithium-ion batteries. ACS Sustainable Chem. Eng. *6*, 1504–1521. https://doi.org/10.1021/acssuschemeng.7b03811.

7. Yu, J., Wang, X., Zhou, M., and Wang, Q. (2019). A redox targeting-based material recycling strategy for spent lithium ion batteries. Energy Environ. Sci. *12*, 2672–2677. https://doi.org/10.1039/C9EE01478K.

8. Velázquez-Martínez, M., Valio, J., Santasalo-Aarnio, A., Reuter, M., and Serna-Guerrero, R. (2019). A critical review of lithium-ion battery recycling processes from a circular economy perspective. Batteries *5*. https://doi.org/10.3390/batteries5040068.

9. Zheng, R., Wang, W., Dai, Y., Ma, Q., Liu, Y., Mu, D., Li, R., Ren, J., and Dai, C. (2017). A closed-loop process for recycling LiNi x Co y Mn (1−x−y) O2 from mixed cathode materials of lithium-ion batteries. Green Energy Environ *2*, 42–50. https://doi.org/10.1016/j.gee.2016.11.010.

10. Yao, L., Feng, Y., and Xi, G. (2015). A new method for the synthesis of LiNi1/3Co1/3Mn1/3O2 from waste lithium ion batteries. RSC Adv *5*, 44107–44114. https://doi.org/10.1039/C4RA16390G.

11. Zhang, X., Bian, Y., Xu, S., Fan, E., Xue, Q., Guan, Y., Wu, F., Li, L., and Chen, R. (2018). Innovative application of acid leaching to regenerate Li(Ni1/3Co1/3Mn1/3)O2 cathodes from spent lithium-ion batteries. ACS Sustainable Chem. Eng. *6*, 5959–5968. https://doi.org/10.1021/acssuschemeng.7b04373.

12. Yang, Y., Xu, S., and He, Y. (2017). Lithium recycling and cathode material regeneration from acid leach liquor of spent lithium-ion battery via facile co-extraction and co-precipitation processes. Waste Manag *64*, 219–227. https://doi.org/10.1016/j.wasman.2017.03.018.

13. Li, L., Bian, Y., Zhang, X., Guan, Y., Fan, E., Wu, F., and Chen, R. (2018). Process for recycling mixed-cathode materials from spent lithium-ion batteries and kinetics of leaching. Waste Manag *71*, 362–371. https://doi.org/10.1016/j.wasman.2017.10.028.

14. Li, L., Fan, E., Guan, Y., Zhang, X., Xue, Q., Wei, L., Wu, F., and Chen, R. (2017). Sustainable recovery of cathode materials from spent lithium-ion batteries using lactic acid leaching system. ACS Sustainable Chem. Eng. *5*, 5224–5233. https://doi.org/10.1021/acssuschemeng.7b00571.

15. Song, X., Hu, T., Liang, C., Long, H.L., Zhou, L., Song, W., You, L., Wu, Z.S., and Liu, J.W. (2017). Direct regeneration of cathode materials from spent lithium iron phosphate batteries using a solid phase sintering method. RSC Adv *7*, 4783–4790. https://doi.org/10.1039/C6RA27210J.

16. Chen, S., He, T., Lu, Y., Su, Y., Tian, J., Li, N., Chen, G., Bao, L., and Wu, F. (2016). Renovation of LiCoO 2 with outstanding cycling stability by thermal treatment with Li 2 CO 3 from spent Li-ion batteries. J. Energy Storage *8*, 262–273. https://doi.org/10.1016/j.est.2016.10.008.

17. Sa, Q., Gratz, E., He, M., Lu, W., Apelian, D., and Wang, Y. (2015). Synthesis of high performance LiNi 1/3 Mn 1/3 Co 1/3 O 2 from lithium ion battery recovery stream. J. Power Sources *282*, 140–145. https://doi.org/10.1016/j.jpowsour.2015.02.046.

18. Sa, Q., Gratz, E., Heelan, J.A., Ma, S., Apelian, D., and Wang, Y. (2016). Synthesis of diverse LiNixMnyCozO2 cathode materials from lithium ion battery recovery stream. J. Sustain. Metall. *2*, 248–256. https://doi.org/10.1007/s40831-016-0052-x.

19. Gratz, E., Sa, Q., Apelian, D., and Wang, Y. (2014). A closed loop process for recycling spent lithium ion batteries. J. Power Sources *262*, 255–262.

20. Zou, H.Y., Gratz, E., Apelian, D., and Wang, Y. (2013). A novel method to recycle mixed cathode materials for lithium ion batteries. Green Chem *15*, 1183–1191.

21. Zheng, Z., Chen, M., Wang, Q., Zhang, Y., Ma, X., Shen, C., Xu, D., Liu, J., Liu, Y., Gionet, P., et al. (2018). High performance cathode recovery from different electric vehicle recycling streams. ACS Sustainable Chem. Eng. *6*, 13977–13982. https://doi.org/10.1021/acssuschemeng.8b02405.

22. Heelan, J., Gratz, E., Zheng, Z., Wang, Q., Chen, M., Apelian, D., and Wang, Y. (2016). Current and prospective Li-ion battery recycling and recovery processes. JOM *68*, 2632–2638.

23. Ma, X., Chen, M., Chen, B., Meng, Z., and Wang, Y. (2019). High-performance graphite recovered from spent lithium-ion batteries. ACS Sustainable Chem. Eng. *7*, 19732–19738. https://doi.org/10.1021/acssuschemeng.9b05003.

24. Chen, B., Ma, X., Chen, M., Bullen, D., Wang, J., Arsenault, R., and Wang, Y. (2019). Systematic comparison of Al 3+ modified LiNi $_{0.6}$ Mn $_{0.2}$ Co $_{0.2}$ O $_2$ cathode material from recycling process. ACS Appl. Energy Mater. *2*, 8818–8825. https://doi.org/10.1021/acsaem.9b01814.

25. Yang, C.-K., Qi, L.-Y., Zuo, Z., Wang, R.-N., Ye, M., Lu, J., and Zhou, H.-H. (2016). Insights into the inner structure of high-nickel agglomerate as high-performance lithium-ion cathodes. J. Power Sources *331*, 487–494. https://doi.org/10.1016/j.jpowsour.2016.09.068.

26. Mao, Y., Wang, X., Xia, S., Zhang, K., Wei, C., Bak, S., Shadike, Z., Liu, X., Yang, Y., Xu, R., et al. (2019). High-voltage charging-induced strain, heterogeneity, and micro-cracks in secondary particles of a nickel-rich layered cathode material. Adv. Funct. Mater. *29*. https://doi.org/10.1002/adfm.201900247.

27. Zheng, J., Ye, Y., Liu, T., Xiao, Y., Wang, C., Wang, F., and Pan, F. (2019). Ni/Li disordering in layered transition metal oxide: electrochemical impact, origin, and control. Acc. Chem. Res. *52*, 2201–2209. https://doi.org/10.1021/acs.accounts.9b00033.

28. Christophersen, J.P. (2014). U.S. department of energy vehicle technologies program: battery test manual for plug-in hybrid electric vehicles. https://doi.org/10.2172/1169249.

29. Xu, C., Märker, K., Lee, J., Mahadevegowda, A., Reeves, P.J., Day, S.J., Groh, M.F., Emge, S.P., Ducati, C., Layla Mehdi, B., et al. (2021). Bulk fatigue induced by surface reconstruction in layered Ni-rich cathodes for Li-ion batteries. Nat. Mater. *20*, 84–92. https://doi.org/10.1038/s41563-020-0767-8.

30. Maleki Kheimeh Sari, H., and Li, X. (2019). Controllable cathode–electrolyte interface of Li[Ni 0.8 Co 0.1 Mn 0.1]O 2 for lithium ion batteries: a review. Adv. Energy Mater. *9*, 1901597. https://doi.org/10.1002/aenm.201901597.

31. Yan, P., Zheng, J., Gu, M., Xiao, J., Zhang, J.G., and Wang, C.M. (2017). Intragranular cracking as a critical barrier for high-voltage usage of layer-structured cathode for lithium-ion batteries. Nat. Commun. *8*, 14101. https://doi.org/10.1038/ncomms14101.

32. Li, T., Yuan, X.-Z., Zhang, L., Song, D., Shi, K., and Bock, C. (2020). Degradation mechanisms and mitigation strategies of nickel-rich NMC-based lithium-ion batteries. Electrochem. Energ. Rev. *3*, 43–80. https://doi.org/10.1007/s41918-019-00053-3.

33. Besli, M.M., Xia, S., Kuppan, S., Huang, Y., Metzger, M., Shukla, A.K., Schneider, G., Hellstrom, S., Christensen, J., Doeff, M.M., et al. (2019). Mesoscale chemomechanical interplay of the LiNi 0.8 Co 0.15 Al 0.05 O 2 cathode in solid-state polymer batteries. Chem. Mater. *31*, 491–501. https://doi.org/10.1021/acs.chemmater.8b04418.

34. Zhang, Y., Zhao, C., and Guo, Z. (2019). Simulation of crack behavior of secondary particles in Li-ion battery electrodes during lithiation/de-lithiation cycles. Int. J. Mech. Sci. *155*, 178–186. https://doi.org/10.1016/j.ijmecsci.2019.02.042.

35. Qian, G., Zhang, Y., Li, L., Zhang, R., Xu, J., Cheng, Z., Xie, S., Wang, H., Rao, Q., He, Y., et al. (2020). Single-crystal nickel-rich layered-oxide battery cathode materials: synthesis, electrochemistry, and intra-granular fracture. Energy Storage Mater *27*, 140–149. https://doi.org/10.1016/j.ensm.2020.01.027.

36. Wandt, J., Freiberg, A., Thomas, R., Gorlin, Y., Siebel, A., Jung, R., Gasteiger, H.A., and Tromp, M. (2016). Transition metal dissolution and deposition in Li-ion batteries investigated by operando X-ray absorption spectroscopy. J. Mater. Chem. A *4*, 18300–18305. https://doi.org/10.1039/C6TA08865A.

37. Li, X., Ren, Z., Norouzi Banis, M., Deng, S., Zhao, Y., Sun, Q., Wang, C., Yang, X., Li, W., Liang, J., et al. (2019). Unravelling the chemistry and microstructure evolution of a cathodic interface in sulfide-based all-solid-state Li-ion batteries. ACS Energy Lett *4*, 2480–2488. https://doi.org/10.1021/acsenergylett.9b01676.

38. Schwieters, T., Evertz, M., Fengler, A., Börner, M., Dagger, T., Stenzel, Y., Harte, P., Winter, M., and Nowak, S. (2018). Visualizing elemental deposition patterns on carbonaceous anodes from lithium ion batteries: a laser ablation-inductively coupled plasma-mass spectrometry study on factors influencing the deposition of lithium, nickel, manganese and cobalt after dissolution and migration from the Li 1 [Ni 1/3 Mn 1/3 Co 1/3]O 2 and LiMn 1.5 Ni 0.5 O 4 cathode. J. Power Sources *380*, 194–201. https://doi.org/10.1016/j.jpowsour.2018.01.088.

39. Wei, C., Xia, S., Huang, H., Mao, Y., Pianetta, P., and Liu, Y. (2018). Mesoscale battery science: the behavior of electrode particles caught on a multispectral X-ray camera. Acc. Chem. Res. *51*, 2484–2492. https://doi.org/10.1021/acs.accounts.8b00123.

40. Wang, J., Karen Chen-Wiegart, Y.C., Eng, C., Shen, Q., and Wang, J. (2016). Visualization of anisotropic-isotropic phase transformation dynamics in battery electrode particles. Nat. Commun. *7*, 12372. https://doi.org/10.1038/ncomms12372.

41. Hong, L., Li, L., Chen-Wiegart, Y.K., Wang, J., Xiang, K., Gan, L., Li, W., Meng, F., Wang, F., Wang, J., et al. (2017). Two-dimensional lithium diffusion behavior and probable hybrid phase transformation kinetics in olivine lithium iron phosphate. Nat. Commun. *8*, 1194. https://doi.org/10.1038/s41467-017-01315-8.

42. Ge, M., and Lee, W.K. (2020). PyXAS - an open-source package for 2D X-ray near-edge spectroscopy analysis. J. Synchrotron Radiat. *27*, 567–575. https://doi.org/10.1107/S1600577520001071.

43. Gürsoy, D., De Carlo, F., Xiao, X., and Jacobsen, C. (2014). TomoPy: a framework for the analysis of synchrotron tomographic data. J. Synchrotron Radiat. *21*, 1188–1193. https://doi.org/10.1107/S1600577514013939.

44. Smekens, J., Paulsen, J., Yang, W., Omar, N., Deconinck, J., Hubin, A., and Van Mierlo, J. (2015). A Modified Multiphysics model for lithium-ion batteries with a LixNi1/3Mn1/3Co1/3O2 electrode. Electrochim. Acta *174*, 615–624. https://doi.org/10.1016/j.electacta.2015.06.015.